

Identifying Switching of Antiferromagnets by Spin-Orbit Torques

Martin Jourdan,^{1,*} Jonathan Bläßer,¹ Guzmán Orero Gámez,¹ Sonka Reimers,¹ Lukas Odenbreit,¹ Miriam Fischer,¹ Yuran Niu,² Evangelos Golias,² Francesco Maccherozzi,³ Armin Kleibert,⁴ Hermann Stoll,^{1,5} and Mathias Kläui¹

¹*Institut für Physik, Johannes Gutenberg-Universität, Staudinger Weg 7, 55128 Mainz, Germany*

²*MAX IV Laboratory, Fotongatan 8, 22484 Lund, Sweden*

³*Diamond Light Source, Chilton OX11 0DE, United Kingdom*

⁴*Paul Scherrer Institut, CH-5232 Villigen PSI, Switzerland*

⁵*Max Planck Institute for Intelligent Systems, Heisenbergstr. 3, 70569 Stuttgart, Germany*

Antiferromagnets are promising candidates for ultrafast spintronic applications, leveraging current-induced spin-orbit torques. However, experimentally distinguishing between different switching mechanisms of the staggered magnetization (Néel vector) driven by current pulses remains a challenge. In an exemplary study of the collinear antiferromagnetic compound Mn_2Au , we demonstrate that slower thermomagnetoelastic effects predominantly govern switching over a wide parameter range. In the regime of short current pulses in the nanosecond range, however, we observe fully Néel spin-orbit torque driven switching. We show that this ultrafast mechanism enables the complete directional alignment of the Néel vector by current pulses in device structures.

* email: Jourdan@uni-mainz.de

INTRODUCTION

Antiferromagnets (AFMs) have been proposed as a groundbreaking platform in spintronics, enabling information storage through the encoding of data in the alignment of the staggered magnetization, also termed Néel vector [1–4]. The integration of antiferromagnets (AFMs) as active components in spintronic devices offers significant advantages, including remarkable stability against external magnetic fields [5], and, most notably, intrinsically fast terahertz (THz) dynamics [6].

Most approaches to the information-writing process, specifically the realignment of the Néel vector, focus on leveraging current pulse-induced spin-orbit torques (SOTs), as this mechanism is anticipated to enable a potentially ultrafast operation. Rotation of the Néel vector is envisioned to be driven by a strong exchange torque, generated when the AFM sublattices are tilted out of their originally antiparallel alignment [2]. In principle, such spin-orbit torques (SOTs) can arise from interfaces between antiferromagnets (AFMs) and non-magnetic heavy metals, as well as from the bulk of metallic AFMs with inversion symmetry breaking in their combined crystallographic and magnetic structure, a mechanism referred to as Néel spin-orbit torque (NSOT) [7–9].

However, experimental evidence for the contribution of NSOTs to current-induced Néel vector reorientation remains limited. These indications primarily consists of observations of current-polarity-dependent motion in a small fraction of domain walls in CuMnAs [10, 11] and Mn_2Au [12], and in a complex directional dependence of small domain modifications in NiO/Pt [13].

On the other hand, an alternative effect has been identified that also induces Néel vector reorientation in anti-

ferromagnets, albeit at a much slower rate compared to SOT-driven processes. This thermomagnetoelastic mechanism arises from current-induced heating, which generates strain and modifies the magnetic anisotropy, ultimately leading to Néel vector reorientation [14, 15]. Distinguishing between these two mechanisms is challenging, yet it is crucial to experimentally verify that current pulse-driven SOT can serve as an ultrafast switching mechanism in antiferromagnetic spintronics.

In this study, we focus on tetragonal Mn_2Au [16], which shows collinear AFM ordering with four equivalent easy $\langle 110 \rangle$ -directions. An NSOT was predicted for this exemplary compound [7], however, it was also shown that its AFM domain configuration also be modified by externally applied strain [17, 18].

We investigate current pulse driven Néel vector switching in Mn_2Au and demonstrate that for pulses of 10 μs or longer, the reorientation process is predominantly driven by the thermomagnetoelastic effect. In contrast, for pulses shorter than 100 ns, we observe switching of AFM domains driven purely by NSOT. Our conclusions are drawn from the analysis of the Néel vector orientation relative to the current direction, which, for a given geometry, exhibits distinct characteristics for the two mechanisms. Additionally, we demonstrate that an effective NSOT results the alignment of the Néel vector along a specific direction, in contrast to the bidirectional alignment observed with a strain-induced easy axis.

RESULTS AND DISCUSSION

Direction of NSOT and thermomagnetoelastic Néel vector reorientation

In this section we will show how the choice of the sample geometry selects either a cooperation or a competition of the thermomagnetoelastic and of the NSOT switching mechanisms.

The direction of NSOT driven Néel vector reorientation is fully determined by the direction of the driving current \mathbf{J} . Following the derivation by Železný et al. [7], the staggered effective fields $\mathbf{B}^A = -\mathbf{B}^B$ at the AFM sublattices A and B are defined by the cross product of the normal \mathbf{z} on an easy plane and the direction of the in-plane current \mathbf{J} :

$$\begin{aligned}\mathbf{B}^A &\propto +\mathbf{z} \times \mathbf{J} \\ \mathbf{B}^B &\propto -\mathbf{z} \times \mathbf{J}\end{aligned}\quad (1)$$

With this staggered effective field, the field like torques \mathbf{T}^A and \mathbf{T}^B act for both AFM sublattices with antiparallel magnetizations $\mathbf{M}^A = -\mathbf{M}^B$ in the same direction, i. e. $\mathbf{T}^A = \mathbf{T}^B$:

$$\begin{aligned}\mathbf{T}^A &\propto \mathbf{M}^A \times (+\mathbf{z} \times \mathbf{J}) \\ \mathbf{T}^B &\propto -\mathbf{M}^A \times (-\mathbf{z} \times \mathbf{J})\end{aligned}\quad (2)$$

The resulting canting of the sublattice magnetizations in the same direction out of the easy-plane generates an exchange torque driven rotation of the Néel vector around \mathbf{z} , whose direction depends on the canting direction [2]. $\mathbf{T}^{A/B}$ is maximum for antiparallel/ parallel alignment and zero for perpendicular alignment of the Néel vector to the current direction. If the magnetization directions of the AFM sublattices are swapped ($\mathbf{M}^{A/B} \rightarrow -\mathbf{M}^{A/B}$), corresponding to a sign change of the Néel vector, the torques change sign as well as shown in Eq. 2.

Tetragonal Mn_2Au is characterized by a strong magnetic anisotropy with a hard c -axis. The magnetic anisotropy within the (001)-plane, which is much smaller, favors two mutually orthogonal magnetic easy axes along the $\langle 110 \rangle$ crystallographic directions. This results in a domain configuration of as grown epitaxial $\text{Mn}_2\text{Au}(001)$ thin film of sub- μm^2 sized domains with four $\langle 110 \rangle$ directions of the Néel vector [19]. Based on the discussion above, an NSOT arising from a current parallel to the $[110]$ direction is expected to switch all domains with Néel vectors aligned parallel or antiparallel to this direction, not only perpendicular to the current but also into the same direction, such as the $[1\bar{1}0]$ direction. As no NSOT acts on the domains with Néel vectors aligned perpendicular to the current direction, those with Néel vectors pointing in the antiparallel $[\bar{1}10]$ direction are unaffected, and 180° domain walls will persist. However, these domain walls are expected to be eliminated by a second current pulse now applied along the $[1\bar{1}0]$ direction, as the NSOT will again rotate the antiparallel Néel vectors in opposite directions around the thin film normal by 90° . Thus, NSOT is characterized by the complete alignment of the Néel, resulting in the formation of one large AFM domain within the active area of a switching device.

In contrast, the thermomagnetoelastic mechanism results in the formation of one axis, along which the Néel vector aligns both parallel and antiparallel, i. e. it favors the formation of 180° domains. Thermomagnetoelastic

switching arises from current-induced heating and the resulting anisotropic thermal expansion of patterned thin-film samples clamped to thick insulating substrates. This can be illustrated by considering a thin, patterned metallic stripe heated by a current pulse. The normal thermal expansion of the stripe, associated with its temperature increase, is constrained by its clamping to the substrate, resulting in strain. However, this constraint is stronger in the direction parallel to the stripe than in the perpendicular direction, leading to compressive strain along the stripe. Thus, the magnetic anisotropy is modified, driving a reorientation of the Néel vector. The axis of thermomagnetoelastic Néel vector alignment depends on the specific device geometry, as demonstrate below through simulations. Consequently, it can be either parallel or perpendicular to the current direction, depending on the sample geometry, which serves as a clear criterion for distinguishing it from NSOT-driven Néel vector reorientation.

The direction of the strain resulting from a current pulse along a specific crystallographic direction can be varied by selecting an appropriate sample geometry. This means that the axis along which the thermomagnetoelastic effect aligns the Néel vector is adjustable, in contrast to the case of the NSOT mechanism, which always aligns the Néel vector perpendicular to the current direction. The typical geometry for current induced Néel vector switching is cross-shaped. As shown in Fig. 1, this cross can be oriented with its arms parallel to the easy $\langle 110 \rangle$ axes (0° cross) or parallel to the in-plane hard $\langle 100 \rangle$ axes (45° cross). In both cases, the current direction in the center of the cross is selected to be parallel to the $[1\bar{1}0]$ direction as shown by the COMSOL [20] simulations in panels **a** and **d** of Fig. 1. The simulated spatially dependent temperature distribution at the end of a current pulse with a width of $10 \mu\text{s}$ is shown in panels **b** and **e**. The corresponding spatial distributions of the strain, i. e. the relative difference in expansion between the $[1\bar{1}0]$ and the $[110]$ directions are shown in panels **c** and **f**. Please note that the sign of strain is different for the two geometries, i. e. the centers of the crosses are strained (elongated) for the 0° cross perpendicular and for the 45° cross parallel to the current direction. Furthermore, the absolute value of the current heating induced strain is about a factor of five smaller for the 45° cross geometry. The magnitude of the strain generally decreases with decreasing pulse widths and current density.

Imaging the switched domain configuration

We now present the corresponding experimental results, obtained by investigating patterned epitaxial $\text{Mn}_2\text{Au}(001)$ thin films using X-ray magnetic linear dichroism – photoelectron emission microscopy (XMLD-PEEM, see *Methods*). The XMLD signal, measured at the Mn-L_{2,3}-edge, ideally produces a black-and-white

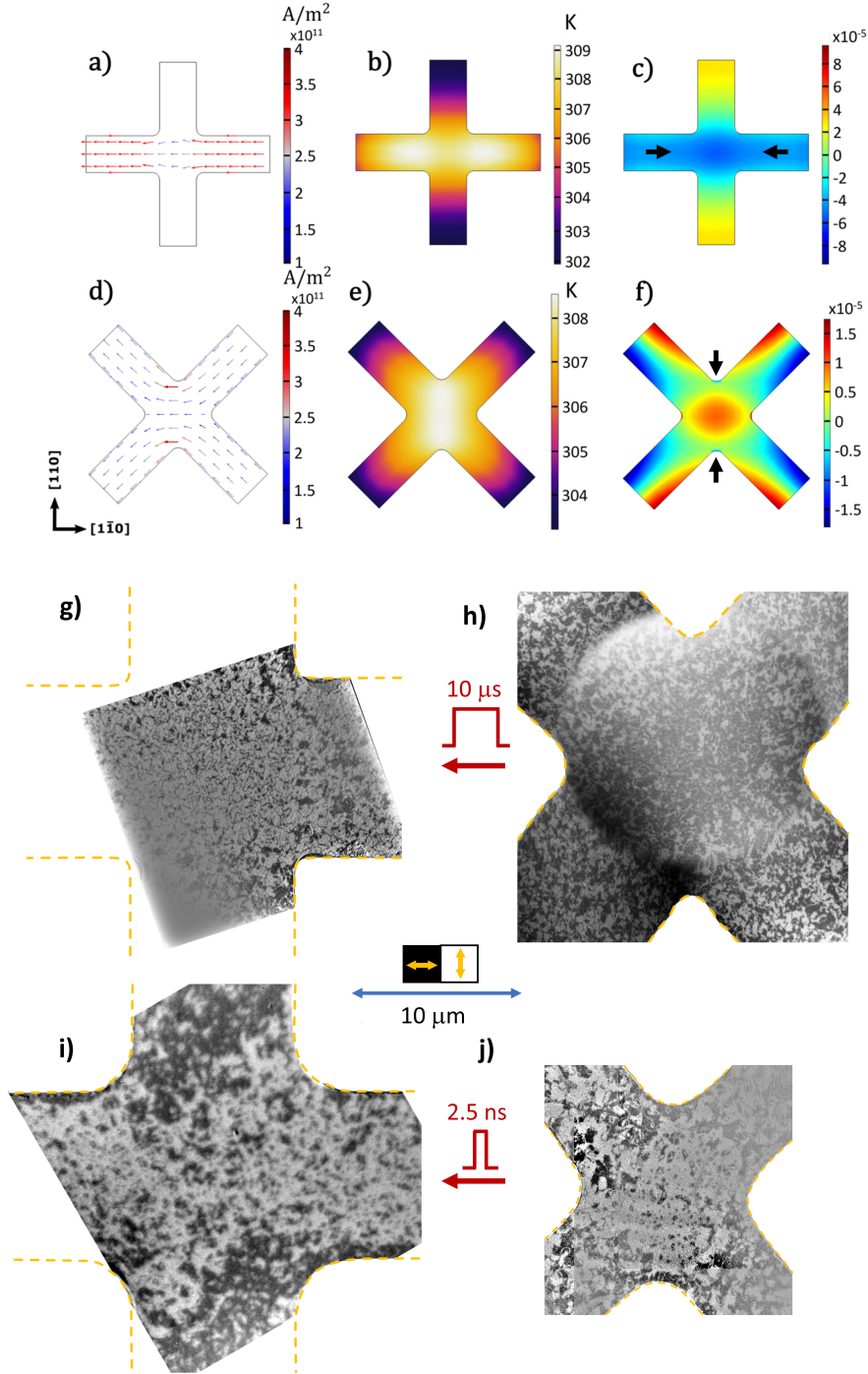


FIG. 1. **Simulations and XMLD-PEEM images of current induced Néel vector reorientation.** The top row (panels a–c) presents COMSOL [20] simulations for a 0° cross configuration. In panel a, the current flows from the right arm to the left arm, panel b shows the associated temperature distribution after a $10 \mu\text{s}$ pulse, and panel c depicts the resulting strain (black arrows), represented as the difference in relative expansion between the $[1\bar{1}0]$ and $[110]$ directions (see color-bar). Panels d–f display the corresponding simulations for a cross rotated by 45° relative to the easy directions, where the current flows from both right arms to both left arms. Panels g and h (composed of 5 images) provide XMLD-PEEM images for experimental comparison of the two geometries after a $10 \mu\text{s}$ pulse, while panels i and j show the corresponding images following a 2.5 ns pulse. The dimensions of the cross shown in panel j are reduced to enable larger current densities.

contrast for the perpendicular $\langle 110 \rangle$ -axes along which the Néel vector is aligned. However, due to a small but unavoidable small energy dispersion of the photon beam over the illuminated sample area, the observed XMLD contrast exhibits spatial variation over the images.

The as-prepared AFM domain configuration of the epitaxial $\text{Mn}_2\text{Au}(001)$ thin films is discussed in detail in Ref. [21]; a typical example, featuring an equal population of sub- μm^2 sized domains, each with the Néel vector aligned along one of the four easy $\langle 110 \rangle$ -directions, is presented in Fig. S1 of the Supplementary Information.

All switched samples shown here were initially pulsed along one of the easy $\langle 110 \rangle$ -directions, followed by pulses along a perpendicular easy direction.

Fig. 1, panels **g** to **j** display magnetic microscopy images of the AFM domain configuration obtained after applying current pulses with variable length in the configurations shown in panels **a** and **d**. In the XMLD-PEEM setup, horizontal alignment of the Néel vector appears dark, while vertical alignment appears bright.

Current pulses with a duration of $10 \mu\text{s}$, applied along the same crystallographic $[1\bar{1}0]$ direction, result in a strong predominance of domains with the Néel vector aligned perpendicular to the current direction (bright) for the 0° cross configuration shown in panel **g**. In contrast, for the 45° cross configuration shown in panel **h**, the Néel vector orientation parallel to the current direction (dark) is dominant. This means that the same current pulse direction leads to mutually perpendicular alignment of the Néel vector in the center of the 0° and 45° crosses, corresponding to the perpendicular directions of the current-induced strain shown in panels **c** and **f**. Thus, these results provide strong evidence for the thermomagnetoelastic switching mechanism. Moreover, our experiments rule out NSOT as the driver of the reorientation process for pulse widths of $10 \mu\text{s}$ or longer (see also Supplementary Information, Fig. S2), as the direction of the NSOT depends solely on the current direction.

However, for current pulses with a length of 2.5 ns , both centers of the 0° and the 45° crosses shown in panels **i** and **j**, display a strong predominance of Néel vector aligned perpendicular to the current direction by appearing bright in the XMLD-PEEM images. This result rules out the thermomagnetoelastic switching mechanism but is fully consistent with NSOT driven Néel vector reorientation.

Compelling evidence for NSOT-induced switching by nanosecond current pulses is provided by the observation of a predominantly single large domain in the center of the 45° cross, as shown in Fig. 1j. This is because NSOT drives the Néel vector to align along a specific direction removing 180° domain walls. In contrast, after a $10 \mu\text{s}$ pulse, the center of the thermomagnetoelastically switched cross contains multiple domain walls with a width close to the resolution limit in the XMLD-PEEM image as shown in Fig. 1g.

To directly visualize the alignment of the Néel vector after the 2.5 ns pulses, we have additionally investigated 45° crosses of $\text{Mn}_2\text{Au}(40 \text{ nm})/\text{Ni}_{80}\text{Fe}_{20}(4 \text{ nm})$ bilayers. As described in ref. [19], these bilayers exhibit a strong collinear exchange coupling between the Néel vector and the magnetization of the ferromagnetic $\text{Ni}_{80}\text{Fe}_{20}$. By leveraging this coupling, we indirectly determine the direction of the Néel vector using XMCD-PEEM at the Fe edge, which reveals the orientation of the $\text{Ni}_{80}\text{Fe}_{20}$ magnetization (Fig. 2, panels **a** and **b**). XMLD-PEEM at the Mn edge (panel **c**) confirms the assumed one-to-one correspondence between the AFM and FM domains also in the switched state.

These results highlight the unique capability of the NSOT to fully align the Néel vector and thereby to create a large single AFM domain from an initially multidomain state.

Electric characterization of switching

We employed both XMLD-PEEM imaging and anisotropic magnetoresistance measurements, associated with Néel vector reorientation, to identify the switched states (see *Methods*). Thermomagnetoelastic Néel vector reorientation was observed for current pulse durations of 1 ms (Supplementary Information, Fig. S2) and $10 \mu\text{s}$ (Fig. 1h). In this regime, current pulses were applied in situ within the PEEM, enabling microscopic observation of changes in the AFM domain structure immediately after each pulse as the current density increased. Pulse widths in the range of $10 \mu\text{s}$ to 100 ns were applied outside the PEEM, as the sample stage wiring within the microscope does not support the impedance matching necessary for these shorter pulses. To pre-characterize the switched state, we measured the transverse resistance of the samples prior to PEEM imaging. After each pulse application at progressively increasing current densities, the transverse resistance (planar Hall effect) was recorded. In these measurements, the increasing fraction of the switched area at the center of the cross-shaped devices is reflected as a corresponding increase or decrease in resistance. Once the resistance change saturates, the sample is considered fully switched and can be imaged ex situ using XMLD-PEEM.

Complete NSOT switching was observed at current densities ranging from $2 \times 10^{12} \text{ A/m}^2$ (100 ns pulses) to $3 \times 10^{12} \text{ A/m}^2$ (2.5 ns pulses) as shown in Fig. 3, panel **a**. These values exceed by more than a factor of five the current density of $4 \times 10^{11} \text{ A/m}^2$ required for thermomagnetoelastic switching with $10 \mu\text{s}$ pulses. As the thermally generated strain induced by current pulses decreases with shorter pulse widths, thermomagnetoelastically driven switching eventually requires higher current densities than NSOT switching. Consistent with this behavior, for a pulse width of 100 ns , we observed NSOT switching at lower current densities, followed by thermomagnetoelastic switching at higher current

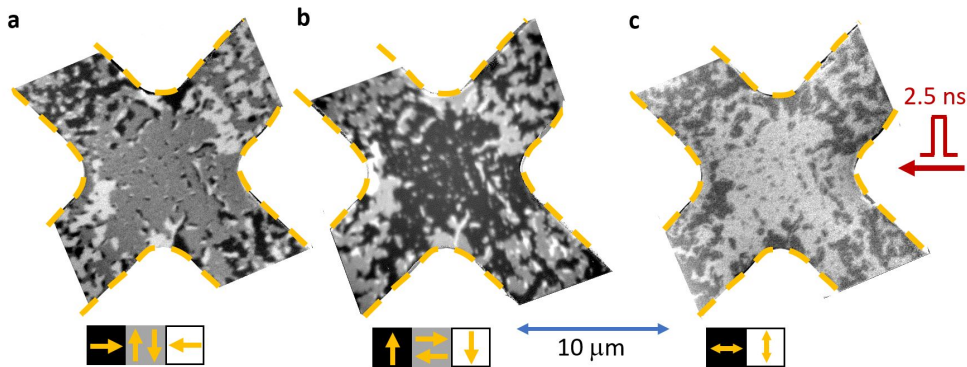


FIG. 2. XMCD- and XMLD-PEEM images of current induced Néel vector reorientation of $\text{Mn}_2\text{Au}/\text{Ni}_{80}\text{Fe}_{20}$. Panels **a** and **b** show the magnetization orientation of the $\text{Ni}_{80}\text{Fe}_{20}$ as obtained through XMCD-PEEM imaging at the Fe-edge, with two different x-ray incidence directions. Panel **c** represents the corresponding XMLD-PEEM image at the Mn-edge, captured after 2.5 ns current pulses, as indicated in the figure.

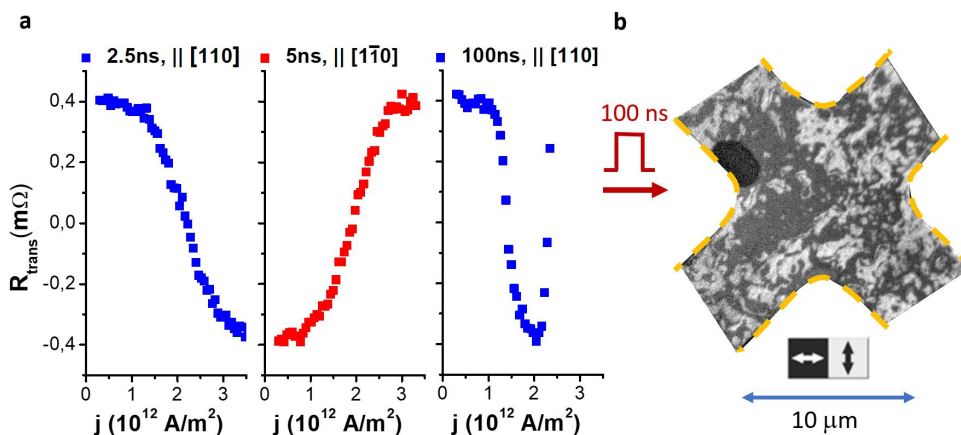


FIG. 3. Effect of Néel vector reorientation on the Mn_2Au resistance and reversed switching. Panel **a** shows the transverse resistance of a 45° Mn_2Au cross in response to sequences of current pulses along alternating perpendicular easy directions, with the pulse width indicated in the figure. After the final pulse sequence with a width of 100 ns, which resulted in a reversal of the resistance change, the sample was imaged using XMLD-PEEM, as shown in panel **b**.

densities, as indicated by the transverse resistance measurements in Fig. 3a. For 100 ns pulse widths, the induced resistance changes initially follow the behavior observed for nanosecond pulses but subsequently reverse sign. In this regime, saturation of the resistance change could not be achieved, as several samples failed under further increases in current density. However, the XMLD-PEEM image shown in Fig. 3b, captured after completing the pulse sequence depicted in panel **a**, clearly reveals a Néel vector alignment parallel to the current direction in the central region of the sample, consistent with expectations for thermomagnetoelastic switching.

Summary & Conclusion

In principle, all current pulse-induced magnetization switching in spintronics is associated with heating effects that generate strain. In epitaxial thin films, strain modi-

fies the magnetocrystalline anisotropy of the investigated compound, ultimately leading to switching. Thus, when studying novel and potentially relatively weak switching mechanisms, such as SOTs acting on AFMs, it is essential to avoid confusion with the thermomagnetoelastic mechanism.

In the context of antiferromagnetic spintronics, the thermomagnetoelastic mechanism is inherently useful, as it in principle enables the switching of all collinear AFMs with multiple easy axes. However, its speed is limited because heat and strain must propagate across the active area of the devices. Thus, achieving ultrafast processes necessitate SOT-driven dynamics.

The compound Mn_2Au is particularly noteworthy for its ability to exhibit both thermomagnetoelastic as well as NSOT switching within the same sample, facilitating their identification. We investigated Néel vector switching in two distinct thin-film geometries, enabling a clear

separation of the two mechanisms. Specifically, in the 45°-cross geometry, thermally induced strain and the predicted NSOT act in opposition. For current pulse widths in the millisecond and microsecond ranges, we observed a directional dependence of the Néel vector reorientation that is consistent with the thermal mechanism alone. However, a transition to NSOT switching is observed for pulse widths in the nanosecond range. In this regime, the Néel vector aligns along a specific direction perpendicular to the current, which is a characteristic feature of the NSOT and could enabling novel applications in spintronics.

Our experiments provide compelling evidence that the current-induced bulk NSOT, predicted ten years ago [7], is sufficiently large to enable Néel vector switching in Mn₂Au devices. Therefore, despite the identification of often dominant thermomagnetoelastic switching, our results strongly support the fundamental viability of SOT-driven switching in AFM spintronics.

METHODS

All experimental data shown in this manuscript were obtained investigating Mn₂Au(001)(45 nm) thin films grown epitaxially on Ta(001)(13 nm)/Mo(001)(20 nm) double buffer layers on MgO(100) substrates. All layers were deposited by magnetron sputtering by the process described in detail in ref. [22]. The samples were capped with 2 nm of polycrystalline SiN_x to protect them from oxidation. Optical lithography and ion beam etching were used to pattern the films into cross-shaped 50 Ω matched coplanar wave guide structures as shown in the Supplementary Information (Fig. S3).

Antiferromagnetic domain imaging was performed by combining photoemission electron microscopy with x-ray magnetic linear dichroism (XMLD-PEEM) at the Mn L_{2,3} absorption edge at the PEEM endstations at beamline MAXPEEM at MAX IV, and beamline I06 at Diamond Light Source, and at the SIM beamline of the Swiss Light Source. The XMLD effect at the Mn L_{2,3} absorption edge in Mn₂Au was established in previous work [19, 23]. For x-ray polarisation along a Mn₂Au ⟨110⟩ direction, the Mn L_{2,3} XMLD spectrum shows a minimum and a maximum located at the absorption edge E_{max} and at 0.8 eV below the edge. At MAXPEEM, the x-ray beam has normal incidence at the sample surface. At I06 and SIM, the x-ray beam is incident at a grazing angle of 16°. The XMCD-PEEM images of Ni₈₀Fe₂₀ were obtained at I06 based on the x-ray magnetic circular dichroism at the Fe absorption edge.

In-situ electrical manipulation was performed at MAXPEEM using the pulse functions of a Keithley2601B-PULSE source for 10 μs and at SIM using a Keithley 2430 (at Diamond) sourcemeters for 1 ms pulses, integrated into the X-PEEM setup.

The ex-situ pulsing in the 100 ns to 2.5 ns range was performed using a Siglent SDG7102A 2-channel arbitrary waveform generator driving two Mini-Circuits LZY-22+ HF amplifiers. The in this frequency range required 50Ω impedance matching was obtained by using a coplanar waveguide design of the Mn₂Au thin films as shown in Fig. S4 of the Supplementary Information, by bonding the sample with short wire-bonds onto a coplanar waveguide sample holder and by using exclusively coaxial cable connections.

The ex-situ resistance measurements (Fig. 3) were performed using a Keithley 6220 precision current source with a probe current of 100 μA and a Keithley 2182A Nanovoltmeter in Delta mode averaging over 100 measurements to obtain one data point. For automatising the pulse - probe sequence Teledyne CR33S30 HF-relays were used.

Acknowledgements

We acknowledge funding by the Deutsche Forschungsgemeinschaft (DFG, German Research Foundation) - TRR 173 - 268565370 (project A05 (M.J.), with contributions from A01 and B02, by the EU HORIZON-CL4-2021-DIGITAL-EMERGING-01-14 programme under grant agreement No. 101070287 (SWAN-on-chip) and by the TopDyn Center (M.K.). We acknowledge MAX IV Laboratory for time on beamline MAXPEEM under Proposals 20230305 and 20240253 (M.J.), Diamond Light Source for time on beamline I06 under proposal MM37862-1 (M.J.), and Swiss Light Source for time on beamline SIM (M.J.). Research conducted at MAX IV, a Swedish national user facility, is supported by the Swedish Research council under contract 2018-07152, the Swedish Governmental Agency for Innovation Systems under contract 2018-04969, and Formas under contract 2019-02496.

Author contributions M.J. wrote the paper and coordinated the project; J.B., G.O.G., S.R. and M.J. prepared the samples and performed the current pulsing and resistance measurements; J.B., G.O.G., S.R., L.O., M.F. and M.J. performed the X-PEEM investigations supported by Y.R.N, E.G., F.M., and A.K.; H.S. supported the development of the HF-pulsing set-up; M.K. contributed to the discussion of the results and provided input.

Competing interests:

The authors declare no competing financial interests.

* Jourdan@uni-mainz.de

[1] MacDonald, A. H., and Tsoi, M. Antiferromagnetic

- Metal Spintronics. *Philos. Trans. R. Soc. A* **369**, 3098 (2011).
- [2] Baltz, V., Manchon, A., Tsoi, M., Moriyama, T., Ono, T., and Tserkovnyak, Y. Antiferromagnetic Spintronics. *Rev. Mod. Phys.* **90**, 015005 (2018).
- [3] Jungwirth, T., Sinova, J., Manchon, A., Marti, X., Wunderlich, J. and Felser, C. The multiple directions of antiferromagnetic spintronics, *Nat. Phys.* **14**, 200 (2018).
- [4] Jungfleisch, M. B., Zhang, W., and Hoffmann, A. Perspectives of antiferromagnetic spintronics, *Phys. Lett. A* **382**, 865 (2018).
- [5] Sapozhnik, A. A., Filianina, M., Bodnar, S. Yu., Lami-rand, A., Mawass, M.-A., Skourski, Y., Elmers, H.-J., Zabel, H., Kläui, M., and Jourdan, M. Direct imaging of antiferromagnetic domains in Mn₂Au manipulated by high magnetic fields. *Phys. Rev. B* **97**, 134429 (2018).
- [6] Kampfrath, T., Sell, A., Klatt, G., Pashkin, A., Mährlein, S., Dekorsy, T., Wolf, M., Fiebig, M., Leitenstorfer, A., and Huber, R. Coherent terahertz control of antiferromagnetic spin waves, *Nat. Photonics* **5**, 31 (2011).
- [7] Železný, J., Gao, H., Výměrný, K., Zemen, J., Mäsek, J., Manchon, A., Wunderlich, J., Sinova, J., and Jungwirth, T. Relativistic Néel-Order Fields Induced by Electrical Current in Antiferromagnets, *Phys. Rev. Lett.* **113**, 157201 (2014).
- [8] Salemi, L., Berritta, M., Nandy, A., K., Oppeneer, P. M. Orbitally dominated Rashba-Edelstein effect in noncentrosymmetric antiferromagnets. *Nat. Commun.* **10**, 5201 (2019).
- [9] Selzer, S., Salemi, L., Deák, A., Szunyogh, L., Oppeneer, P., M., and Nowak, U., Current-induced switching of antiferromagnetic order in Mn₂Au from first principles. *Phys. Rev. B* **105**, 174416 (2022).
- [10] Wadley, P., Reimers, S., Grzybowski, M. J., Andrews, C., Wang, M., Chauhan, J. S., Gallagher, B. L., Campion, R. P., Edmonds, K. W., Dhési, S. S., Maccherozzi, F., Novák, V., Wunderlich, J., and Jungwirth, T. Current polarity-dependent manipulation of antiferromagnetic domains *Nat. Nanotech.* **13**, 632 (2018).
- [11] Amin, O. J., Reimers, S., Maccherozzi, F., Dhési, S. S., Novák, V., Campion, R. P., Edmonds, K. W., Wadley, P. Electrical control of 180° domain walls in an antiferromagnet. *APL Materials* **11**, 091112 (2023).
- [12] Reimers, S., Lytvynenko, Y., Niu, Y. R., Golias, E., Sarpi, B., Veiga, L. S. I., Denneulin, T., Kovács, A., Dunin-Borkowski, R. E., Kläui, M., Jourdan, M. Current-driven writing process in antiferromagnetic Mn₂Au for memory applications. *Nat. Commun.* **3630** 1861 (2023).
- [13] Schmitt, C., Rajan, A., Beneke, G., Kumar, A. Sparmann, T., Meer, H., Bednarz, B., Ramos, R., Nino, M. A., Foerster, M., Saitoh, E., Kläui, M. Mechanisms of electrical switching of ultra-thin CoO/Pt bilayers. *Nano Lett.* **24**, 1471 (2024).
- [14] Baldrati, L.; Schmitt, C.; Gomonay, O.; Lebrun, R.; Ramos, R.; Saitoh, E.; Sinova, J.; Kläui, M. Efficient Spin Torques in Antiferromagnetic CoO/Pt Quantified by Comparing Field- and Current-Induced Switching. *Phys. Rev. Lett.* **125**, 077201 (2020).
- [15] Meer, H., Schreiber, F., Schmitt, C., Ramos, R., Saitoh, E., Gomonay, O., Sinova, J., Baldrati, L., and Kläui, M. Direct Imaging of Current-Induced Antiferromagnetic Switching Revealing a Pure Thermomagnetoelastic Switching Mechanism in NiO. *Nano Lett.* **21**, 114 (2021).
- [16] Barthem, V. M. T. S., Colin, C. V., Mayaffre, H., Julien, M.-H., and Givord, D. Revealing the properties of Mn₂Au for antiferromagnetic spintronics. *Nat. Commun.* **4**, 2892 (2013).
- [17] Chen, X., Zhou, X., Cheng, R., Song, C., Zhang, J., Wu, Y., Ba, Y., Li, H., Sun, Y., You, Y., Zhao, Y., and Pan, F., Electric field control of Néel spin-orbit torque in an antiferromagnet. *Nat. Mater.* **18**, 931 (2019).
- [18] Grigorev, V., Filianina, M., Lytvynenko, Y., Sobolev, S., Pokharel, A. R., Lanz, A. P., Sapozhnik, A., Kleibert, A., Bodnar, S., Grigorev, P., Skourski, Y., Kläui, M., Elmers, H.-J., Jourdan, M. and Demsar, J., Optically Triggered Néel Vector Manipulation of a Metallic Antiferromagnet Mn₂Au under Strain. *ACS Nano* **16**, 20589, (2022).
- [19] Bommanaboyena, S. P., Backes, D., Veiga, L. S. I., Dhési, S. S., Niu, Y. R., Sarpi, B., Denneulin, T., Kovács, A., Mashoff, T., Gomonay, O., Sinova, J., Everschor-Sitte, K., Schönke, D., Reeve, R. M., Kläui, M., Elmers, H.-J., and Jourdan, M., Readout of an antiferromagnetic spintronics system by strong exchange coupling of Mn₂Au and Permalloy. *Nat. Commun.* **12**, 2829 (2021).
- [20] www.comsol.com
- [21] Reimers, S., Gomonay, O., Amin, O. J., Krizek, F., Barton, L. X., Lytvynenko, Y., Poole, S. F., Novák, V., Campion, R. P., Maccherozzi, F., Carbone, G. Björling, A., Niu, Y., Golias, E., Kriegner, D., Sinova, J., Kläui, Jourdan, M., Dhési, S. S., Edmonds, K. W., Wadley, P., Magnetic domain engineering in antiferromagnetic CuMnAs and Mn₂Au. *Phys. Rev. Appl.* **21**, 064030 (2024).
- [22] Bomammaboyena, S. P., Bergfeldt, T., Heller, R., Kläui, M., and Jourdan, M. High quality epitaxial Mn₂Au (001) thin films grown by Molecular Beam Epitaxy. *J. Appl. Phys.* **127**, 243901 (2020).
- [23] Sapozhnik, A. A., Abrudan, R., Skourski, Jourdan, M., Yu., Zabel, H., Kläui, Elmers, H. J. Manipulation of antiferromagnetic domain distribution in Mn₂Au by ultrahigh magnetic fields and by strain. *Phys. Stat. Sol. (RRL)* **11**, 1600438 (2017).

SUPPLEMENTARY INFORMATION

AFM domain configurations of $\text{Mn}_2\text{Au}(001)$

Figure S1 shows an XMLD-PEEM image illustrating a typical domain configuration in as-grown $\text{Mn}_2\text{Au}(001)$ epitaxial thin films prior to the application of current pulses. After switching the same sample with a $10\ \mu\text{s}$ current pulse, the resulting domain configuration is depicted in Fig. 1g of the main manuscript.

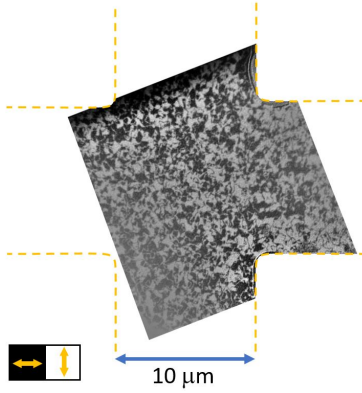


FIG. 4. S1: XMLD-PEEM image of the AFM domain pattern of a Mn_2Au thin film before any current injection.

The longest current pulses used to switch 45° Mn_2Au crosses had a width of 1 ms. An XMLD-PEEM image of a sample switched under these conditions is shown in Fig. S2. This result aligns with Fig. 1h of the main manuscript, as in both cases, the Néel vector becomes aligned parallel to the current direction, indicating thermomagnetoelastic switching. The required current density for 1 ms pulses is slightly lower than that for $10\ \mu\text{s}$ pulses, amounting to $2.6 \times 10^{11}\ \text{A}/\text{m}^2$.

Sample geometry & pulse connections

For current pulse durations in the nanosecond range, proper impedance matching to $50\ \Omega$ is required.

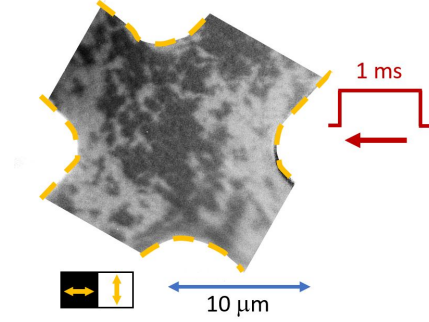


FIG. 5. S2: XMLD-PEEM image of a Mn_2Au 45° cross switched with a 1 ms current pulse.

Therefore, the samples were patterned using a coplanar waveguide geometry, as shown in Fig. S3. For pulsing with the current flowing horizontally through the center of the 45° cross, two current pulses with positive polarity are simultaneously applied to the right arms, while two current pulses with negative polarity are applied to the left arms.

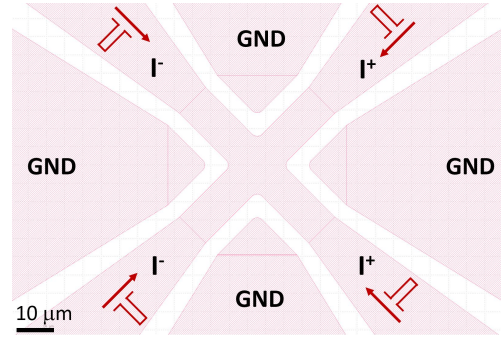


FIG. 6. S3: Sample geometry for nanosecond current pulsing with electrical connections.